Single-crystal elasticity of (Al,Fe)-bearing bridgmanite up to 82 GPa

Suyu Fu[1,*], Yanyao Zhang[1], Takuo Okuchi[2,‡], and Jung-Fu Lin[1,†]

[1]Department of Geological Sciences, Jackson School of Geosciences, The University of Texas at Austin, Austin, Texas 78712, U.S.A.
[2]Institute for Planetary Materials, Okayama University, Misasa, Tottori 682-0193, Japan

Abstract

Thermoelastic properties of mantle candidate minerals are essential to our understanding of geophysical phenomena, geochemistry, and geodynamic evolutions of the silicate Earth. However, the lower-mantle mineralogy remains much debated due to the lack of single-crystal elastic moduli (C_{ij}) and aggregate sound velocities of (Al,Fe)-bearing bridgmanite, the most abundant mineral of the planet, at the lower mantle pressure-temperature (P-T) conditions. Here we report single-crystal C_{ij} of (Al,Fe)-bearing bridgmanite, $Mg_{0.88}Fe_{0.1}Al_{0.14}Si_{0.90}O_3$ (Fe10-Al14-Bgm) with $Fe^{3+}/\Sigma Fe = \sim0.65$, up to ~82 GPa using X-ray diffraction (XRD), Brillouin light scattering (BLS), and impulsive stimulated light scattering (ISLS) measurements in diamond-anvil cells (DACs). Two crystal platelets with orientations of (–0.50, 0.05, –0.86) and (0.65, –0.59, 0.48), that are sensitive to deriving all nine C_{ij}, are used for compressional and shear wave velocity (v_P and v_S) measurements as a function of azimuthal angles over 200° at each experimental pressure. Our results show that all C_{ij} of singe-crystal Fe10-Al14-Bgm increase monotonically with pressure with small uncertainties of 1–2% (±1σ), except C_{55} and C_{23}, which have uncertainties of 3–4%. Using the third-order Eulerian finite-strain equations to model the elasticity data yields the aggregate adiabatic bulk and shear moduli and respective pressure derivatives at the reference pressure of 25 GPa: $K_S = 326 \pm 4$ GPa, $\mu = 211 \pm 2$ GPa, $K_S' = 3.32 \pm 0.04$, and $\mu' = 1.66 \pm 0.02$ GPa. The high-pressure aggregate v_S and v_P of Fe10-Al14-Bgm are 2.6–3.5% and 3.1–4.7% lower than those of $MgSiO_3$ bridgmanite end-member, respectively. These data are used with literature reports on bridgmanite with different Fe and Al contents to quantitatively evaluate pressure and compositional effects on their elastic properties. Comparing with one-dimensional seismic profiles, our modeled velocity profiles of major lower-mantle mineral assemblages at relevant P-T suggest that the lower mantle could likely consist of about 89 vol% (Al,Fe)-bearing bridgmanite. After considering uncertainties, our best-fit model is still indistinguishable from pyrolitic or chondritic models.

Keywords: Single-crystal elasticity, bridgmanite, lower mantle, pyrolite, chondrite

Introduction

Earth's lower mantle, the most voluminous region of the planet, plays a key role in regulating physical, chemical, and dynamic interactions between the core and upper mantle as well as the crust. Geochemical and petrological observations indicate that the upper mantle likely consists of pyrolite with approximately three portions of peridotite and one portion of basalt (Ringwood 1975). If one assumes the whole mantle is chemically homogenous in major elements, a pyrolitic lower mantle would have ~75 vol% (Al,Fe)-bearing bridgmanite [(Mg,Fe,Al),(Fe,Al,Si)O_3, Bgm], ~18 vol% ferropericlase [(Mg,Fe)O, Fp], and ~7 vol% CaSiO$_3$ davemaoite (Irifune et al. 2010; Tschauner et al. 2021). However, such a pyrolitic model with Mg/Si = ~1.25 has much less Si than the chondritic bulk Earth model with Mg/Si = ~1.0 from cosmochemical constraints (McDonough and Sun 1995). To address the "missing Si" conundrum in the silicate Earth,

Si as a light element in the core (Allègre et al. 1995) and/or a Si-rich lower mantle (Hofmann 1997) have been proposed previously. Moreover, some recent studies suggest that comparisons of velocity and density profiles between seismic observations (Dziewonski and Anderson 1981; Kennett et al. 1995) and mineral physics models (Irifune et al. 2010; Kurnosov et al. 2017; Mashino et al. 2020; Murakami et al. 2012) could provide important insights into the lower-mantle mineralogy. This would require a complete and reliable elasticity data set of the lower-mantle candidate minerals with small uncertainties.

Bridgmanite is suggested to be the most abundant lower-mantle mineral (Ringwood 1975). Despite extensive theoretical studies on its elasticity at high P-T (Karki et al. 1997; Shukla and Wentzcovitch 2016; Wentzcovitch et al. 2004), experimental investigations on this subject are still limited to polycrystalline samples or single crystals at relatively low pressures. In addition, as much as 10 mol% Fe^{3+} and Al^{3+} could substitute the dodecahedral-site (A-site) Mg^{2+} and octahedral-site (B-site) Si^{4+} in the crystal structure of bridgmanite via charge-coupled substitution (e.g., Frost et al. 2004; McCammon 1997), whose effects on the elastic properties also need investigation. Of particular examples are the reports by Murakami et al. (2012)

---

* Present address: School of Earth and Space Exploration, Arizona State University, Tempe, Arizona, U.S.A. Co-Corresponding Author E-mail: fsyxhy@gmail.com
† Co-Corresponding Author E-mail: afu@jsg.utexas.edu
‡ Present address: Institute for Integrated Radiation and Nuclear Science, Kyoto University, Kyoto, Japan. E-mail: fafu@jsg.utexas.edu

and Mashino et al. (2020) that measured v_S of polycrystalline Al- and/or Fe-bearing bridgmanite up to 124 GPa using BLS technique to suggest a perovskitic lower mantle with greater than 92 vol% bridgmanite. A recent study measured both v_P and v_S of polycrystalline Fe-bearing bridgmanite, $Mg_{0.96}Fe^{2+}_{0.036}Fe^{3+}_{0.014}Si_{0.99}O_3$, up to 70 GPa at 300 K using both ISLS and BLS methods and observed a drastic softening in v_P at 42.6–58 GPa and a slight increase in v_S above 40 GPa (Fu et al. 2018). This finding has been attributed to the spin transition of B-site Fe^{3+} in bridgmanite (Fu et al. 2018; Shukla et al. 2016). However, the sound velocity data from polycrystalline samples in DACs to represent their bulk properties has been questioned in Earth science because of issues with velocity anisotropies, textures, and direction-dependent acoustic phonon intensities (Speziale et al. 2014).

As to single-crystal elasticity study, Criniti et al. (2021) and Kurnosov et al. (2017) measured velocities in BLS experiments to determine single-crystal elasticity of $MgSiO_3$ and (Al,Fe)-bearing bridgmanite, $Mg_{0.9}Fe_{0.1}Al_{0.1}Si_{0.9}O_3$ (Fe10-Al10-Bgm), up to 79 and 40 GPa, respectively. Due to the technical limitation in BLS measurements where v_P peaks of bridgmanite can be blocked by diamond v_S signals above 20 GPa, these studies (Criniti et al. 2021; Kurnosov et al. 2017) used a global fit scheme by fitting all the velocity data together to derive single-crystal C_{ij} at high pressure. It has been debated whether such a global fit scheme is appropriate because those greater uncertainties of derived C_{ij} at higher pressures were compensated by higher quality data at lower pressures (Kurnosov et al. 2018; Lin et al. 2018). To improve the full elasticity data, a recent study determined single-crystal elasticity of (Al,Fe)-bearing bridgmanite with two compositions, $Mg_{0.95}Fe^{2+}_{0.033}Fe^{3+}_{0.027}Al_{0.04}Si_{0.96}O_3$ (Fe6-Al4-Bgm) and $Mg_{0.89}Fe^{2+}_{0.024}Fe^{3+}_{0.096}Al_{0.11}Si_{0.89}O_3$ (Fe12-Al11-Bgm), by individually fitting velocity data from both ISLS and BLS measurements at each experimental pressure of 25 and 35 GPa (Fu et al. 2019b). The results showed that the coupled substitution of Fe and Al in bridgmanite significantly decreases its v_P and v_S. In a nutshell, because of the lack of single-crystal elasticity data of (Al,Fe)-bearing bridgmanite across the whole lower-mantle pressure, it has been a great challenge for a better understanding of the lower-mantle composition and seismic observations.

Here, we reported single-crystal C_{ij} of (Al,Fe)-bearing bridgmanite, $Mg_{0.88}Fe_{0.1}Al_{0.14}Si_{0.90}O_3$ (Fe10-Al14-Bgm) with $Fe^{3+}/\Sigma Fe$ = ~0.65, up to ~82 GPa at 300 K using v_P data from ISLS, v_S data from BLS, and pressure-density relationship (equation of state, EoS) from synchrotron XRD measurements in DACs. Two platelets with crystallographic orientations of (–0.50, 0.05, –0.86) and (0.65, –0.59, 0.48) are selected with sufficient sensitivities to derive full C_{ij} with small uncertainties (Fig. 1). The use of ISLS and BLS techniques (Fu et al. 2018; Yang et al. 2015) enables both v_P and v_S measurements on selected platelets as a function of azimuthal angles at high pressure (Fig. 2; Online Materials[1] Fig. S1; Online Materials[1] Table S1), that overcomes previous difficulties when only using BLS technique (Criniti et al. 2021; Kurnosov et al. 2017; Mashino et al. 2020; Murakami et al. 2012). Together with literature reports on elastic properties of bridgmanite with different Al and Fe contents, we can quantitatively evaluate the effect of Fe and Al on its adiabatic bulk and shear moduli (K_S and μ) at high pressure. Our results are used in a self-consistent thermoelastic model to evaluate velocity profiles
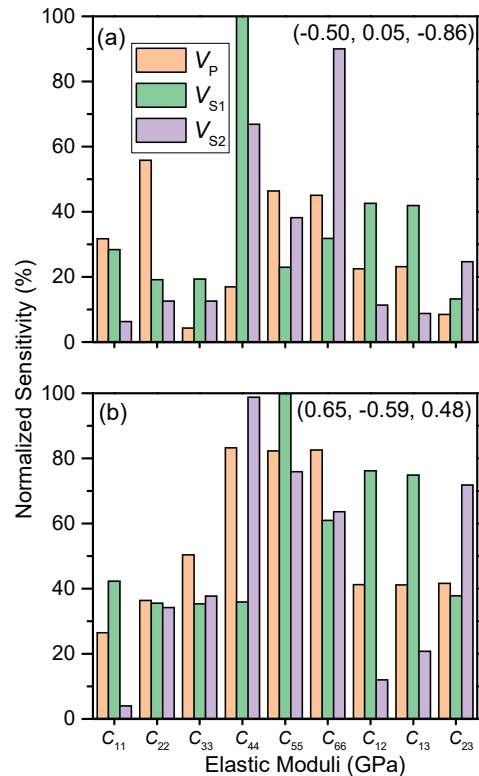
FIGURE 1. Sensitivity analyses of single-crystal bridgmanite platelets for derivations of its elastic moduli. (**a** and **b**) Platelets with crystallographic orientations of (–0.50, 0.05, –0.86) and (0.65, –0.59, 0.48), respectively. The calculations follow literature studies (Fu et al. 2019b; Lin et al. 2018) for analyzing sensitivity of nine C_{ij} to experimentally measured v_P, v_{S1}, and v_{S2} in the orthorhombic-structured single-crystal bridgmanite with a selected orientation. (Color online.)

of lower-mantle mineral aggregates at relevant *P-T*, and then applied to help us better constrain the lower-mantle composition.

EXPERIMENTAL METHODS

Single-crystal bridgmanite with run number 5K2667 was synthesized using the 5000 ton Kawai-type multi-anvil apparatus at the Institute for Planetary Materials at Okayama University. Starting materials of magnesium hydroxide [Mg(OH)₂], enstatite [MgSiO₃], aluminum oxide [Al₂O₃], and iron oxide [⁵⁷FeO] were mechanically mixed with desired weight percentages, and were then sealed into a Pt capsule. The Pt capsule in the sample assemblage was compressed and heated up to ~24 GPa and ~1800 °C for 20 h to synthesize single-crystal (Al,Fe)-bearing bridgmanite. Details of sample synthesis and characterizations on its chemistry, $Fe^{3+}/\Sigma Fe$, and crystallinity have been well documented in a previous study (Fu et al. 2019a). Results from electron microprobe analysis, Mössbauer spectroscopy, Raman spectroscopy, transmission electron microscopy, and synchrotron XRD reveal that the synthesized bridgmanite is chemically homogeneous and inclusions-free in micrometer- to nanometer-spatial resolutions with a composition of $Mg_{0.88}Fe_{0.1}Al_{0.14}Si_{0.90}O_3$ and $Fe^{3+}/\Sigma Fe$ = ~0.65. Single-crystal XRD results show sharp diffraction spots with lattice parameters of *a* = 4.7875(3) Å, *b* = 4.9423(2) Å, *c* = 6.9205(6) at ambient conditions, confirming the high quality of single-crystal samples needed for elasticity measurements.

Bridgmanite has an orthorhombic structure (*Pbnm*) in lower-mantle *P-T* with nine independent C_{ij} to be constrained. Following a literature procedure (Fu et al. 2019b), we first selected and double-sided polished several platelets to ~25–30 μm thick using diamond films for synchrotron single-crystal XRD measurements at ambient conditions at 13 ID-D GeoSoilEnviroCARS (GSECARS) of the Advanced

Photon Source (APS), Argonne National Laboratory (ANL). An incident X-ray with a 0.3344 Å wavelength was used for the measurements in which ±15° rotations of each platelet about the vertical axis of the sample stage were employed to determine its crystallographic orientation with an uncertainty of <0.2°. Then, the determined orientation of each platelet was used to calculate its sensitivity of synthetic velocities to C_{ij} so that we can select appropriate platelets for velocity measurements and derivations of full C_{ij} with small uncertainties. Based on these analyses (Fig. 1), two platelets with orientations of (–0.50, 0.05, –0.86) and (0.65, –0.59, 0.48) with sufficient sensitivities were used for velocity measurements.

BLS and ISLS measurements were conducted on the selected platelets loaded into DACs up to 82 GPa with a pressure interval of 6–10 GPa in the Mineral Physics Laboratory of the Department of Geological Sciences at The University of Texas at Austin. Re gaskets with initial thicknesses of 250 μm were pre-indented to 25 GPa or ~28 μm thick using short symmetric 200 μm culet DACs. Pre-indented areas were drilled with 130 μm diameter holes as sample chambers. Selected platelets were cut using focused ion beam into circular shapes (Marquardt and Marquardt 2012), ~60–70 μm in diameter, and were polished down to 10 μm thick to be loaded into sample chambers in two runs. Neon was used as pressure medium and a ruby sphere pressure calibrant was placed close to the sample to minimize pressure uncertainties (Fig. 2c insert). We note that, to achieve pressure stability and ensure pressure consistency between two runs, each DAC was kept at the target experimental pressure for 2–3 days before velocity measurements. Ruby fluorescence was taken before and after each measurement to evaluate pressure uncertainties (Dewaele et al. 2004). We used the ruby pressure scale by Dewaele et al. (2004) because of its internal consistency with the Au pressure scale used in

our complementary XRD experiments. We also note that synchrotron single-crystal XRD of the loaded platelets in DACs were conducted at several high-pressure points at 13 ID-D of GSECARS at APS, ANL. The circular and round diffraction peaks with average FWHM of ~0.04–0.07° confirmed the high quality of our crystals up to 76 GPa in neon medium (Figs. 2a–2b). Analyses of XRD show consistent orientation information with small deviations (<1°) as determined at ambient conditions.

The BLS system is equipped with a solid-state green laser of 532 nm wavelength and a ~30 μm focused beam size (Coherent Verdi V2), a JRS six-pass tandem Fabry-Perot Interferometer, and an APD detector (Laser Components Count-10B). We collected BLS spectra at a forward scattering geometry with an external scattering angle of 48.1°. The ISLS system uses a pump-and-probe technique with an infrared pump laser of 1064 nm wavelength and a green probe laser of 532 nm wavelength. Both lasers have pulse widths of 15 ps and repetition rates of 200 000 Hz. Two excitation beams, that are split from the pump laser, are recombined at the sample position with a crossing angle of 20.3°. The focused probe laser on the sample has a beam size of 30–40 μm. To avoid potential geometrical errors, both BLS and ISLS systems were aligned precisely using a series of reference spots and iris diaphragms, and were calibrated using distilled water and standard glass (Fu et al. 2018). To avoid potential sample degradation due to the metastability of bridgmanite at low pressures, we intentionally started BLS and ISLS measurements from ~24 GPa where bridgmanite is expected to be thermodynamically stable. BLS and ISLS spectra were collected on two loaded samples as a function of azimuthal angles over 200° with a 10° step rotation at each experimental pressure (Online Materials[1] Table S1). Collected BLS spectra were used to derive v_S and time-domain ISLS spectra were Fourier-transformed into frequency-domain power spectra to
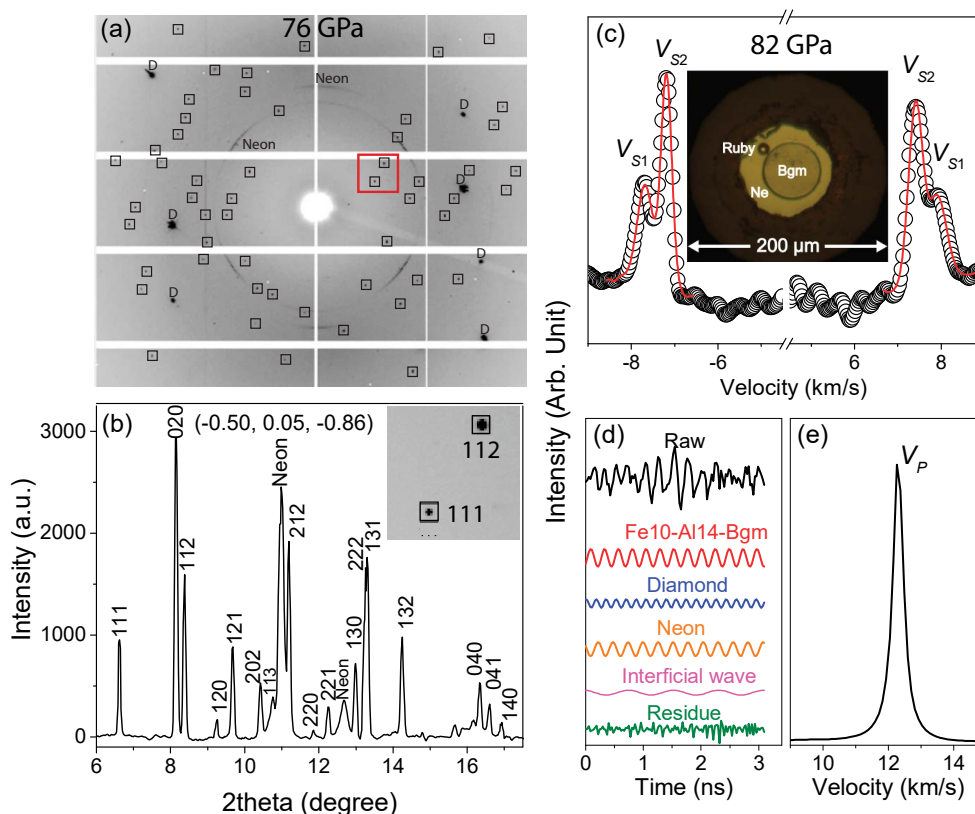
FIGURE 2. High-pressure X-ray diffraction and sound velocity measurements on single-crystal Fe10-Al14-Bgm. (**a**) Original XRD image on single-crystal Fe10-Al14-Bgm at ~76 GPa and 300 K. (**b**) The corresponding integrated pattern. In **a**, diffraction peaks from the sample are marked with a small rectangle, and signals from neon pressure medium and diamonds are labeled with "neon" and "D", respectively. Analyses of the XRD pattern indicate the loaded platelet has a crystallographic orientation of (–0.50, 0.05, –0.86). In **b**, Miller indices (*hkl*) of bridgmanite are labeled close to diffracted peaks. Average FWHM of these peaks are ~0.06°. Insert in **b** is a zoom-in region marked by a red rectangle in **a**, showing nice and round diffraction peaks. (**c**–**e**) Representative BLS, ISLS, and power spectra of single-crystal Fe10-Al14-Bgm at ~82 GPa and 300 K. Open circles in **c** are raw BLS data and red lines are best fits to derive v_{S1} and v_{S2}. A time-domain ISLS spectrum in **d** is Fourier-transformed into a frequency-domain power spectrum in **e** to derive v_P. The insert in **c** shows an image of the sample chamber with the Fe10-Al14-Bgm platelet and a ruby sphere as the pressure calibrant. (Color online.)
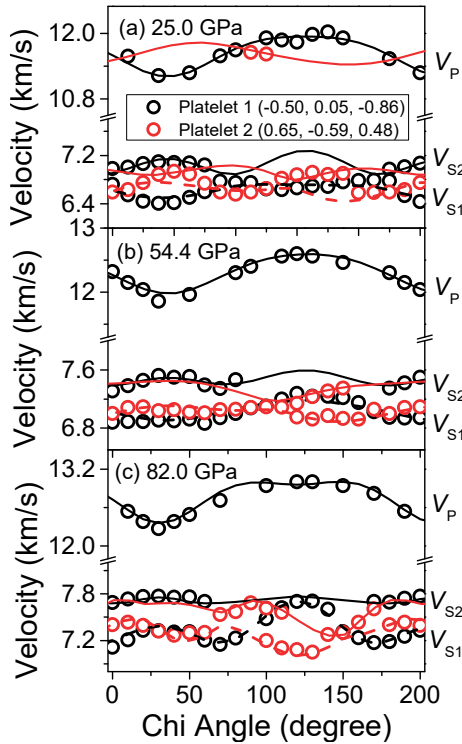
Figure 3. Sound velocities of single-crystal Fe10-Al14-Bgm as a function of azimuthal chi angles at high pressure. (**a**) 25.0 GPa. (**b**) 54.4 GPa. (**c**) 82.0 GPa. Black and red circles are experimentally measured sound velocities of two platelets with crystallographic orientations of (−0.50, 0.05, −0.86) and (0.65, −0.59, 0.48), respectively. Lines are the best fits to derive the full elastic moduli using Christoffel's equations. The two perpendicularly polarized shear wave velocities, v_{S1} and v_{S2}, are plotted as dashed and solid lines, respectively. (Color online.)

derive v_P of the sample at high pressure (Figs. 2c–2e).

A complimentary XRD run was conducted on single-crystal Fe10-Al14-Bgm up to 75 GPa at 300 K to evaluate its pressure-volume relationship at 13 ID-D of GSECARS at APS, ANL (Online Materials[1] Fig. S1; Online Materials[1] Table S2). Here, we followed a previous experimental procedure (Fu et al. 2018) by loading a piece of Fe10-Al14-Bgm platelet, ~20 μm in length and ~8 μm in thickness, into a symmetric DAC with 200 μm culets, together with Au as the pressure calibrant and neon as the pressure medium. These results allow us to calculate the high-pressure density (ρ) of the crystal, which is needed for deriving the full C_{ij}.

RESULTS AND DISCUSSION

Single-crystal elasticity of Fe10-Al14-Bgm at high pressure

The measured BLS and ISLS spectra display high signal-to-noise ratios and are used to derive v_{S1}, v_{S2}, and v_P of single-crystal Fe10-Al14-Bgm up to ~82 GPa (Figs. 2c–2e). We used Christoffel's equations (Every 1980) to fit the obtained velocities as a function of azimuthal angles over a range of 200° and derived the full C_{ij} of single-crystal Fe10-Al14-Bgm at each experimental pressure (Fig. 3):

$$|C_{ijkl}n_jn_j - \rho v^2\delta_{ik}| = 0 \tag{1}$$

where C_{ijkl} is the elastic tensor with full suffix notation, which is contracted to C_{ij} in Voigt form in this study, v are measured velocities of v_P, v_{S1}, and v_{S2}, n_i are wave vector direction co-

sines, and δ_{ik} is the Kronecker delta. Results show that all C_{ij} values increase monotonically with pressure up to 82 GPa with uncertainties (±1σ) of 1–2%, except C_{55} and C_{23} with errors of ~3–4%, which are consistent with our sensitivity test (Fig. 4; Table 1). We note that only BLS measurements were conducted on the platelet of (0.65, −0.59, 0.48) with sufficient v_{S1} and v_{S2} information to shorten the experimental time and decrease the risk of breaking diamonds. Overall, the use of combined BLS and ISLS measurements on two sensitive crystal platelets with extended v_S and v_P datapoints at high pressure assures derivations of all C_{ij} with acceptable uncertainties.

Comparison of the obtained C_{ij} of Fe10-Al14-Bgm with literature studies shows that almost all C_{ij} values except C_{12} have similar pressure dependences to those from theoretical calculations on MgSiO$_3$ bridgmanite (Karki et al. 1997; Li et al. 2005; Wentzcovitch et al. 2004) and those from experimental investigations on MgSiO$_3$ bridgmanite (Criniti et al. 2021) and Fe10-Al10-Bgm (Kurnosov et al. 2017). Compared to MgSiO$_3$ bridgmanite end-member (Criniti et al. 2021), C_{11}, C_{22}, C_{33}, and C_{44} of Fe10-Al14-Bgm are about 8, 7, 6, andd 12% lower, respectively, C_{66} and C_{23} of Fe10-Al14-Bgm displays 10–15% increase, and C_{55} and C_{13} of Fe10-Al14-Bgm show weak changes. We also found that the shear moduli of Fe10-Al14-Bgm show $C_{66} > C_{44}$, which is opposite from the MgSiO$_3$ bridgmanite with $C_{44} > C_{66}$. Early studies have shown that the Fe and Al substitution in bridgmanite can greatly affects its C_{ij}, especially on longitudinal and shear moduli (Fu et al. 2019b; Li et al. 2005). As to the C_{12}, our Fe10-Al14-Bgm has much lower values than theoretical and experimental reports on MgSiO$_3$ bridgmanite at pressures above 40 GPa (Criniti et al. 2021; Karki et al. 1997; Li et al. 2005; Wentzcovitch et al. 2004). It should be noted that the C_{12} of Fe10-Al14-Bgm is comparable to that of Fe10-Al10-Bgm within the overlapped experimental pressure range when using the individual fit scheme (Lin et al. 2018) instead of the global fit (Kurnosov et al. 2017). Criniti et al. (2021) used a global fit scheme to derive the single-crystal C_{ij} of MgSiO$_3$ bridgmanite up to 79 GPa but they can only report reliable C_{ij} below 30 GPa using the individual fit scheme. This is because the individual fit scheme does not work on their velocity data with limited v_P information at pressures above 50 GPa (Criniti et al. 2021). As discussed by Lin et al. (2018), the global fit approach, that takes all the velocity data at high pressure to derive C_{ij} values, would lead to the compensation of C_{ij} errors at higher pressure by the lower pressure data that have lower uncertainties. As demonstrated in our analyses (Figs. 1 and 3), extensive v_P and v_S data points at each experimental pressure are key to deriving C_{ij} values with small uncertainties. Thermoelastic modeling of the C_{ij} values taken from the literature should thus be exercised with caution in error propagations.

To quantitatively derive pressure derivatives of all C_{ij}, we used a finite-strain theory (Stixrude and Lithgow-Bertelloni 2005) to fit these high-pressure results (Fig. 4; Table 2):

$$C_{ij} = (1 + 2f)^{5/2}(C_{ij0} + a_1f + a_2f^2) \tag{2}$$
$$a_1 = (3K_{S0}C'_{ij0} - 5C_{ij0}) \tag{3}$$
$$a_2 = 6K_{S0}C'_{ij0} - 14C_{ij0} - 1.5K_{S0}(3K'_{S0} - 16)\Delta \tag{4}$$
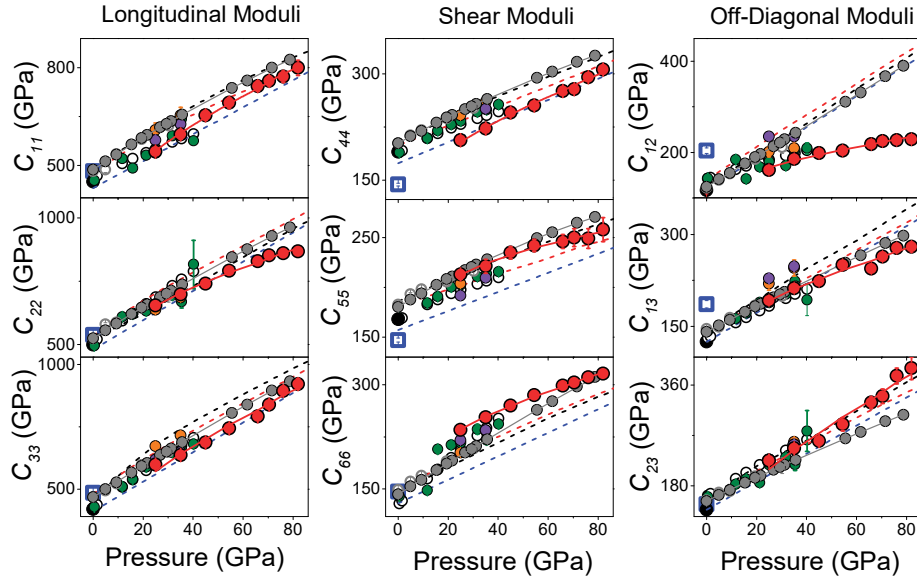
Figure 4. Single-crystal elastic moduli of Fe10-Al14-Bgm as a function of pressure. Solid red circles are C_{ij} results of Fe10-Al14-Bgm in this study, and solid red lines are the best fits to the data using a finite-strain theory (Stixrude and Lithgow-Bertelloni 2005). Literature results on bridgmanite with different compositions are plotted for comparisons. Dashed black (Karki et al. 1997), red (Wentzcovitch et al. 2004), and blue (Li et al. 2005) lines are from ab initio calculations for $MgSiO_3$ bridgmanite. Other symbols are from previous experimental measurements. Open and solid gray circles: $MgSiO_3$ bridgmanite from the individual fit and global fit, respectively, and the solid gray lines are the best finite-strain fits (Criniti et al. 2021); solid orange and purple circles: Fe6-Al4-Bgm and Fe12-Al11-Bgm, respectively (Fu et al. 2019b); open black circles: Fe10-Al10-Bgm using the global fit (Kurnosov et al. 2017); solid olive circles: recalculated individual fit results by Lin et al. (2018) using velocity data of Kurnosov et al. (2017); open blue squares: $MgSiO_3$ bridgmanite (Yeganeh-Haeri 1994); solid black circles: $MgSiO_3$ bridgmanite (Fukui et al. 2016). Errors are smaller than symbols when not shown. (Color online.)

where C'_{ij0} and K'_{S0} are pressure derivatives of single-crystal elastic moduli, C_{ij0}, and adiabatic bulk modulus, K_{S0}, respectively, at the reference pressure, Δ is a constant parameter calculated as $\Delta = -\delta_{ij}\delta_{kl} - \delta_{il}\delta_{jk} - \delta_{jl}\delta_{ik}$, with values of –3 for C_{11}, C_{22}, C_{33}, and of –1 for C_{44}, C_{55}, C_{66}, C_{12}, C_{13}, C_{23}. The Eulerian strain (f) is expressed as:

$$f = \frac{1}{2}[(V_0/V)^{2/3} - 1] \qquad (5)$$

where V_0 is the unit-cell volume at ambient conditions and V is the unit-cell volume at high pressure from XRD measurements (see Online Materials[1]). Here, we used 25 GPa, our initial experimental pressure for velocity measurements, as the reference pressure for the finite-strain fitting because of the thermodynamic

stability of bridgmanite (the same scheme was used for K_S and μ in the following). Our fitting results show that C_{33} has a greater pressure derivative than the other two principle longitudinal moduli of C_{11} and C_{22}, which leads to $C_{33} > C_{22}$ above ~70 GPa (Fig. 4). This is consistent with the trend of $MgSiO_3$ bridgmanite (Criniti et al. 2021) although there are slight variations in the pressure derivatives. On the other hand, the pressure derivatives of shear moduli in Fe10-Al14-Bgm exhibit $C_{44} > C_{66} > C_{55}$. With pressure increasing, the smallest shear modulus at ambient, C_{44}, exceeds C_{55} above 30 GPa and is expected to be $>C_{66}$ at the lowermost mantle pressure. In comparison, among the shear moduli in $MgSiO_3$ bridgmanite, its C_{66} is the smallest at ambient and has the largest pressure derivative: C_{66} is expected to be higher than C_{55} and C_{44} above 40 GPa and megabar pressure,

TABLE 1. Elastic moduli of single-crystal Fe10-Al14-Bgm at high pressures

P (GPa)	25.0(3)	35.0(5)	45.0(5)	54.4(6)	65.8(8)	70.4(7)	76.0(9)	82.0(14)
C_{11} (GPa)	542(9)	596(15)	654(15)	693(16)	743(16)	760(15)	773(17)	800(23)
C_{22} (GPa)	653(3)	697(5)	740(4)	791(5)	829(4)	852(5)	860(6)	868(8)
C_{33} (GPa)	598(9)	636(13)	687(14)	744(15)	793(14)	839(16)	895(18)	922(22)
C_{44} (GPa)	207(2)	223(3)	246(2)	256(3)	276(2)	279(3)	295(5)	306(6)
C_{55} (GPa)	213(5)	221(7)	235(6)	242(5)	246(7)	250(9)	249(10)	258(12)
C_{66} (GPa)	235(3)	253(3)	270(3)	285(4)	299(3)	303(4)	311(4)	316(5)
C_{12} (GPa)	162(5)	186(3)	198(5)	204(6)	218(5)	225(6)	227(6)	229(5)
C_{13} (GPa)	192(4)	212(6)	224(6)	250(5)	245(5)	264(7)	278(8)	280(9)
C_{23} (GPa)	225(5)	247(8)	260(8)	290(12)	329(10)	340(13)	376(14)	390(20)
K_S (GPa)	326(4)	356(5)	382(6)	412(6)	437(8)	455(8)	473(9)	485(11)
μ (GPa)	211(2)	224(2)	242(2)	254(2)	268(3)	273(3)	279(4)	287(5)
ρ (g/cm³)	4.56(1)	4.71(1)	4.83(1)	4.94(2)	5.05(2)	5.10(2)	5.16(2)	5.21(3)
v_P (km/s)	11.52(8)	11.80(8)	12.08(10)	12.33(11)	12.54(12)	12.67(13)	12.79(14)	12.90(16)
v_S (km/s)	6.79(4)	6.90(4)	7.09(5)	7.18(5)	7.28(5)	7.32(5)	7.35(6)	7.42(6)

Note: Errors in parentheses are one standard deviation (±1σ) from standard error propagation analyses.

TABLE 2. Pressure derivatives of single-crystal elasticity (C_{ij}, K_S, and μ) of Fe10-Al14-Bgm modelled using a finite-strain theory

	Fe10-Al14-Bgm (this study)[a]		MgSiO$_3$ (Criniti et al. 2021)[b]		
ij	C_{ij0} (GPa)	C'_{ij0}	C_{ij0} (GPa)	C'_{ij0}	
11	542(9)	5.35(9)	487(2)	5.21(9)	
22	653(3)	4.98(14)	524(3)	6.35(6)	
33	598(9)	6.67(28)	467.7(16)	6.56(6)	
44	207(2)	2.01(6)	202.3(2)	1.95(1)	
55	213(5)	1.11(5)	180.2(4)	1.55(1)	
66	235(3)	1.78(3)	141.9(5)	2.30(1)	
12	162(5)	1.58(7)	124.3(18)	3.27(7)	
13	192(4)	1.85(8)	140.9(13)	2.17(6)	
23	225(5)	2.95(12)	152.6(10)	2.22(3)	
	M_0 (GPa)	M'_0	M_0 (GPa)	M'_0	M''_0 (GPa^{-1})
K^V	328(4)	3.35(5)	257.1(6)	3.71(4)	–0.014
μ^V	212(2)	1.67(2)	175.6(2)	1.86(1)	–0.0174
K^R	325(4)	3.29(4)	256.7(4)	3.70(3)	–0.014
μ^R	210(2)	1.65(2)	174.0(6)	1.86(4)	–0.0173
K^{VRH}	326(4)	3.32(4)	256.9(8)	3.70(5)	–0.014
μ^{VRH}	211(2)	1.66(2)	174.8(7)	1.86(4)	–0.0174

[a] The reference pressure is 25 GPa.
[b] The reference pressure is at ambient conditions.

respectively (Criniti et al. 2021). The off-diagonal moduli of Fe10-Al14-Bgm display $C_{23} > C_{13} > C_{12}$ at all the pressure range with similar trends for their pressure derivatives. In particular, our Fe10-Al14-Bgm has a 50% lower pressure derivative of C_{12} than MgSiO$_3$ bridgmanite (Criniti et al. 2021), which might be due to the use of a global fit scheme by Criniti et al. (2021). Our results on the single-crystal C_{ij} and associated pressure derivatives of Fe10-Al14-Bgm suggest that Fe and Al substitutions play a key role in the elastic properties of bridgmanite. The elasticity of bridgmanite with a relevant Al and Fe composition in the lower mantle is more appropriate for geophysical implications.

Elastic moduli and sound velocities of bridgmanite aggregates at high pressure

K_S and μ of bridgmanite aggregates can be calculated from its single-crystal C_{ij} by using a Voigt-Reuss-Hill averaging scheme (Hill 1952):

$$K_V = [C_{11} + C_{22} + C_{33} + 2(C_{12} + C_{13} + C_{23})]/9 \tag{6}$$

$$K_R = D/E \tag{7}$$

$$K_S = (K_V + K_R)/2 \tag{8}$$

$$\mu_V = [C_{11} + C_{22} + C_{33} + 3(C_{44} + C_{55} + C_{66}) - (C_{12} + C_{13} + C_{23})]/15 \tag{9}$$

$$\mu_R = 15 / \left[\frac{4F}{D} + 3\left(\frac{1}{C_{44}} + \frac{1}{C_{55}} + \frac{1}{C_{66}} \right) \right] \tag{10}$$

$$\mu = (\mu_V + \mu_R)/2 \tag{11}$$

where K_V (μ_V) and K_R (μ_R) are upper Voigt and lower Reuss bounds of K_S (μ), respectively, and D, E, and F are three constants, calculated as:

$$D = C_{13}(C_{12}C_{23} - C_{13}C_{22}) + C_{23}(C_{12}C_{13} - C_{11}C_{23}) + C_{33}(C_{11}C_{22} - C_{12}C_{12}) \tag{12}$$

$$E = C_{11}(C_{22} + C_{33} - 2C_{23}) + C_{22}(C_{33} - 2C_{13}) - 2C_{12}C_{33} + C_{12}(2C_{23} - C_{12}) + C_{13}(2C_{12} - C_{13}) + C_{23}(2C_{13} - C_{23}) \tag{13}$$

$$F = C_{11}(C_{22} + C_{33} + C_{23}) + C_{22}(C_{33} + C_{13}) + C_{12}C_{33} - C_{12}(C_{23} + C_{12}) - C_{13}(C_{12} + C_{13}) - C_{23}(C_{13} + C_{23}) \tag{14}$$

Accordingly, aggregate v_P and v_S of the single-crystal Fe10-Al14-Bgm can be calculated using:

$$v_P = \sqrt{(K_S + 4\mu/3)/\rho} \tag{15}$$

$$v_S = \sqrt{\mu/\rho} \tag{16}$$

Standard derivations ($\pm 1\sigma$) on the elastic moduli and aggregate velocities can be calculated using these equations with standard error propagations. Our results show that aggregate v_S and v_P values of Fe10-Al14-Bgm increase monotonically with pressure up to ~82 GPa with uncertainties <1.0% (Fig. 5). Compared with literature reports on aggregate elastic properties of polycrystalline and single-crystal bridgmanite (Chantel et al. 2012; Criniti et al. 2021; Fu et al. 2019b; Jackson et al. 2005; Karki et al. 1997; Kurnosov et al. 2017; Lin et al. 2018; Murakami et al. 2012), our K_S, μ, v_P, and v_S show generally consistent profiles for the first order and display strong Fe and Al effect: v_S and v_P of Fe10-Al14-Bgm are 2.6 and 3.1% lower than those of MgSiO$_3$ bridgmanite (Criniti et al. 2021), respectively, at 25 GPa and the values increase up to 3.5 and 4.7% for v_S and v_P, respectively, at 80 GPa. This indicates an increasing Fe and Al effect on sound velocities of bridgmanite with pressure. We also notice that the sound velocities of Fe10-Al14-Bgm are comparable to those of Fe10-Al10-Bgm by Kurnosov et al. (2017) within the overlapped experimental pressures of 25–40 GPa due to their similar Fe and Al contents. On the other hand, literature studies suggest that B-site Fe^{3+} in Fe-bearing bridgmanite could undergo a spin transition at approximately 40–60 GPa and cause an abrupt v_P softening (Fu et al. 2018). The monotonical increase of v_S and v_P in our Fe10-Al14-Bgm with pressure up to 82 GPa indicates the possible lack of B-site Fe^{3+} spin transition. This might be due to the fact that the Mg$_{0.88}$Fe$_{0.1}$Al$_{0.14}$Si$_{0.90}$O$_3$ bridgmanite contains ~10% Fe in the A site while 14% Al preferentially stays in the B site (Fu et al. 2019a; Mao et al. 2017).
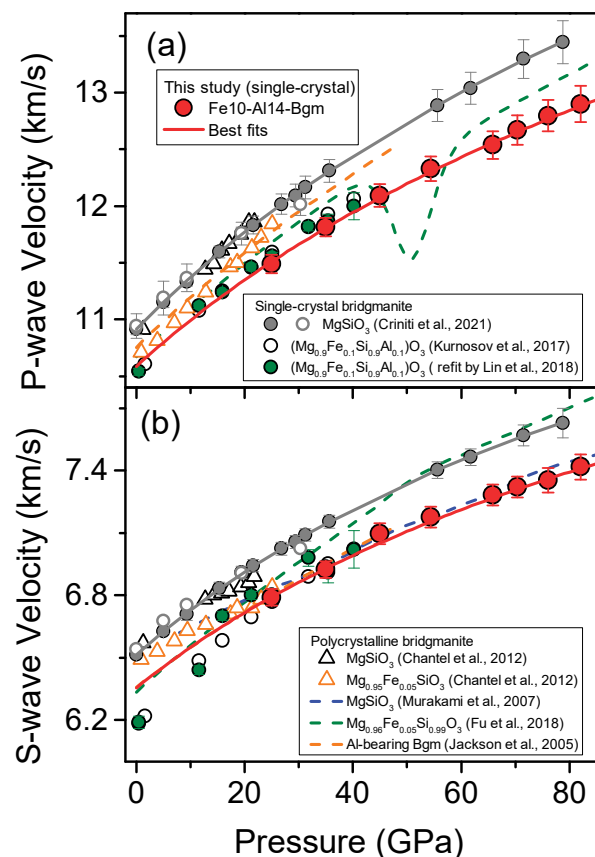
High-pressure aggregate K_S and μ of the Fe10-Al14-Bgm can be fitted using third-order Eulerian finite-strain equations (Stixrude and Lithgow-Bertelloni 2005):

$$K_S = (1 + 2f)^{5/2} [K_{S0} + (3K_{S0}K'_{S0} - 5K_{S0})f + 13.5(K_{S0}K'_{S0} - 4K_{S0})f^2] \tag{17}$$

$$\mu = (1 + 2f)^{5/2} [\mu_0 + (3K_{S0}\mu'_0 - 5\mu_0)f + (6K_{S0}\mu'_0 - 24K_{S0} - 14\mu_0 + 4.5K_{S0}K'_{S0})f^2] \tag{18}$$

where K_{S0} (μ_0) is the adiabatic bulk (shear) modulus at the reference pressure (25 GPa in this study), K'_{S0} (μ'_0) is the pressure derivative of K_{S0} (μ_0). The best fits yield $K_S = 326 \pm 4$ GPa, $\mu = 211 \pm 2$ GPa, $K'_S = 3.32 \pm 0.04$, and $\mu' = 1.66 \pm 0.02$ GPa at 25 GPa (Table 2). These values for Fe10-Al14-Bgm are comparable to literature reports on Al-, Fe-, or (Al,Fe)-bearing bridgmanite (Chantel et al. 2012; Criniti et al. 2021; Jackson et al. 2005; Kurnosov et al. 2017; Murakami et al. 2012) after considering Fe and Al substitution effects, pressure effects, as well as trade-offs between elastic moduli and their pressure derivatives during fitting (Fig. 6;

Table 3). We note that the reference pressure in the literature is typically at ambient conditions (Chantel et al. 2012; Jackson et al. 2005; Kurnosov et al. 2017), while we used the initial experimental pressure of 25 GPa as the reference. We also note that literature studies (Chantel et al. 2012; Jackson et al. 2005; Kurnosov et al. 2017) commonly neglect the term at f^2 order when evaluating the high-pressure elasticity of bridgmanite. Such approximations are acceptable at relatively low pressures (<40 GPa), where the term f^2 is small and neglectable. However, Helmholtz free energy at higher orders increases with pressure and cannot be simply truncated at

Figure 5. Aggregate sound velocities of single-crystal Fe10-Al14-Bgm at high pressure and room temperature. (**a**) v_P. (**b**) v_S. Solid red symbols are aggregate velocity calculated from single-crystal C_{ij} of Fe10-Al14-Bgm in this study, and solid red lines are the best fits using a finite-strain theory (Stixrude and Lithgow-Bertelloni 2005). Other symbols and lines are literature data for different bridgmanite compositions. Particularly, circles are data from single-crystal bridgmanite and triangles and dashed lines are from polycrystalline samples. Open and solid gray circles: single-crystal $MgSiO_3$ bridgmanite from individual and global fits, respectively, and the solid gray lines are the best finite-strain fits (Criniti et al. 2021); open black circles: single-crystal $Mg_{0.9}Fe_{0.1}Si_{0.9}Al_{0.1}O_3$ with $Fe^{3+}/\Sigma Fe = 0.67$ from the global fit (Kurnosov et al. 2017); solid olivine circles: recalculated results by Lin et al. (2018) using the individual fit to the velocity data of Kurnosov et al. (2017); black and orange triangles: polycrystalline $MgSiO_3$ and $Mg_{0.95}Fe_{0.05}SiO_3$ with $Fe^{3+}/\Sigma Fe = 0.2$, respectively (Chantel et al. 2012); dashed blue, olivine, and orange lines: polycrystalline $MgSiO_3$ (Murakami et al. 2007), $Mg_{0.96}Fe_{0.05}Si_{0.99}O_3$ (Fu et al. 2018) and Al-bearing bridgmanite containing 5.1 wt% Al_2O_3 (Jackson et al. 2005), respectively. Uncertainties are smaller than symbols when not shown. (Color online.)

high P-T conditions (Stixrude and Lithgow-Bertelloni 2005). In addition, the EoS data from XRD experiments in literature and this study are used to derive the isothermal bulk modulus (K_{T0}), which is slightly different from K_{S0} from velocity measurements even after the K_{S0}-K_{T0} conversion (Table 3) (Boffa Ballaran et al. 2012; Criniti et al. 2021; Kurnosov et al. 2017; Mao et al. 2017; Murakami et al. 2012). The sensitivity of the bulk moduli to density and velocity data and their errors with different fitting methods will need further evaluation to understand the difference.

Effects of Fe and Al substitution on elastic properties of bridgmanite

Previous studies suggest that Fe and Al cations could enter A-site Mg and B-site Si in the structure of bridgmanite via charge-coupled substitution under lower-mantle P-T and compositional conditions (Irifune et al. 2010; Lin et al. 2013). It is thus important to quantitatively evaluate Fe and Al substitution effects on the elastic properties of bridgmanite aggregates before one can apply elasticity results for lower-mantle implications. Here for simplicity, we assume that both Fe and Al compositional effects on the K_S and μ of bridgmanite are linear. As to the existence of Fe^{2+} and Fe^{3+} in bridgmanite, we take the total Fe effect as the sum of Fe^{2+} and Fe^{3+} contents. With those assumptions, all the literature on high-pressure K_S and μ data of bridgmanite with different compositions (Chantel et al. 2012; Criniti et al. 2021; Fu et al. 2018; Jackson et al. 2005; Kurnosov et al. 2017; Murakami et al. 2012; Murakami et al. 2007) were fit together with the Fe10-Al14-Bgm in this study using third-order Eulerian finite-strain equations (Fig. 6). We note that we only included the velocity data of the Fe-bearing bridgmanite by Fu et al. (2018) at 25–40 GPa range because of the existence of B-site Fe^{3+} spin transition at 40–60 GPa. The best fits yield:

$$K_{S0}(\text{Fe,Al}) = 253 - 118\text{Fe}_{\text{Bgm}} + 64\text{Al}_{\text{Bgm}} \quad (19)$$

$$K'_{S0}(\text{Fe,Al}) = 4.29 + 0.9\text{Fe}_{\text{Bgm}} - 6.05\text{Al}_{\text{Bgm}} \quad (20)$$

$$\mu_0(\text{Fe,Al}) = 174.7 - 4.28\text{Fe}_{\text{Bgm}} - 98.9\text{Al}_{\text{Bgm}} \quad (21)$$

$$\mu'_0(\text{Fe,Al}) = 1.67 + 1.10\text{Fe}_{\text{Bgm}} + 1.24\text{Al}_{\text{Bgm}} \quad (22)$$

where Fe_{Bgm} and Al_{Bgm} are Fe and Al contents in bridgmanite, calculated as $\text{Fe}_{\text{Bgm}} = \text{Fe}/(\text{Fe}+\text{Mg})$ and $\text{Al}_{\text{Bgm}} = \text{Al}/(\text{Al}+\text{Si})$, respectively. We note that 68% of residues of K_S and μ in the best fits are <1.1% and 1.0%, respectively ($\pm 1\sigma$) (Figs. 6c–6d), indicating these evaluations are statistically reliable within uncertainties. The modeled μ_0 and K_{T0} for $MgSiO_3$ bridgmanite end-member are consistent with literature reports within experimental uncertainties (Chantel et al. 2012; Li and Zhang 2005). The modeling shows that the incorporation of Fe into bridgmanite will decrease its K_S and v_P, while Al will increase the K_S and v_P. As to the shear moduli, Al has a much stronger effect on μ and v_S reductions of bridgmanite as compared to Fe incorporation.

IMPLICATIONS

Velocity and density comparisons between seismic observations (Dziewonski and Anderson 1981; Kennett et al. 1995) and mineral physics models (Irifune et al. 2010; Kurnosov et al. 2017; Mashino et al. 2020; Murakami et al. 2012) have been widely used to constrain the lower-mantle mineralogy. For instance, Murakami
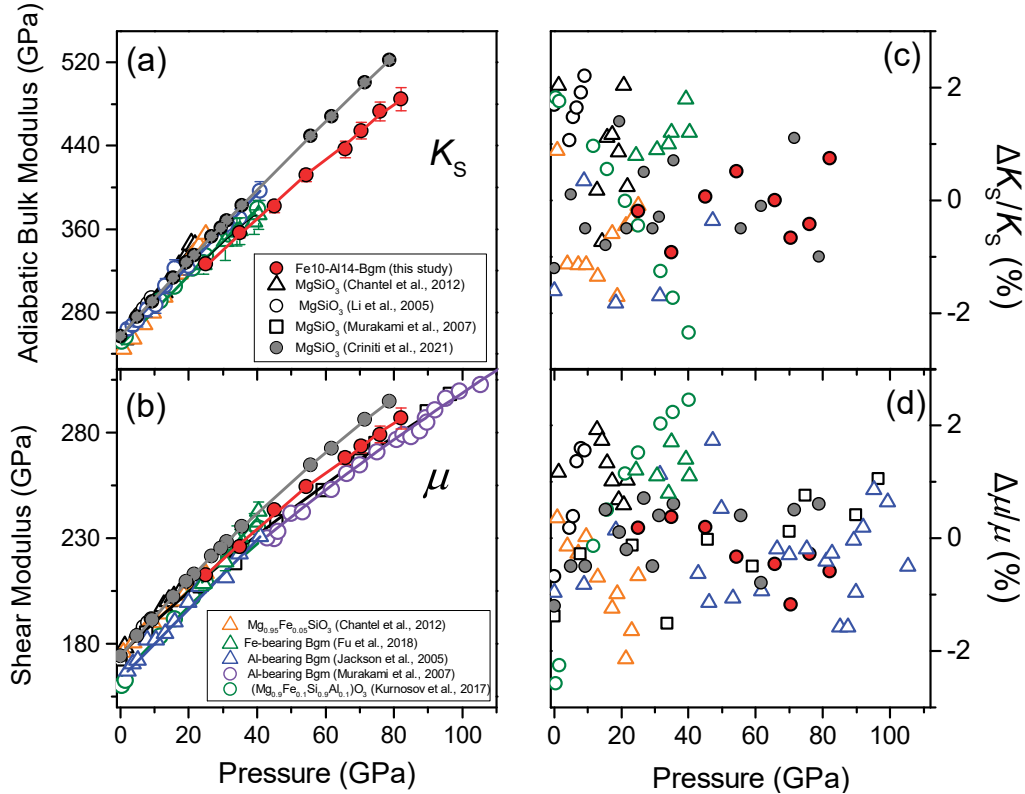
FIGURE 6. Adiabatic bulk and shear moduli of bridgmanite with different Fe and Al contents at high pressure and 300 K. (**a** and **b**) K_S and μ, respectively. Solid red circles are from the single-crystal Fe10-Al14-Bgm data in this study and other symbols are experimental data from the literature (Boffa Ballaran et al. 2012; Chantel et al. 2012; Criniti et al. 2021; Fu et al. 2018; Jackson et al. 2005; Kurnosov et al. 2017; Li and Zhang 2005; Lundin et al. 2008; Mao et al. 2017; Murakami et al. 2012, 2007). Uncertainties are smaller than symbols when not shown. See detailed references in legends. Solid lines with corresponding colors are the best fits to the data using third-order finite-strain equations (Stixrude and Lithgow-Bertelloni 2005) that take Fe and Al substitution effects into account. (**c** and **d**) $\Delta K_S/K_S$ and $\Delta\mu/\mu$, respectively. These are residues in adiabatic bulk and shear moduli between experimental data and the best fits. (Color online.)

et al. (2012) used v_S of polycrystalline Al-bearing bridgmanite up to 124 GPa and 2700 K to suggest >92 vol% bridgmanite in the lower mantle, while Kurnosov et al. (2017) suggested a Fe^{3+}-rich pyrolitic lower mantle above 1200 km depth from single-crystal elasticity data of Fe10-Al10-Bgm up to 40 GPa at 300 K. However, it has been pointed out by Cottaar et al. (2014) that the conclusion of a perovskitic lower mantle (Murakami et al. 2012) was not supported because of the use of inconsistent thermoelastic modeling and inappropriate averaging schemes for mineral aggregates. Here we have adopted a self-consistent thermoelastic model within the framework of Mie-Grüneisen thermal EoS and finite-strain theory (Jackson and Rigden 1996; Stixrude and Lithgow-Bertelloni 2005) to evaluate lower-mantle mineralogy at the extended lower-mantle depth.

Modeling of velocity profiles of one-phase bridgmanite in the lower mantle

The high P-T K_S and μ of an individual phase can be calculated using self-consistent thermoelastic equations:

$$P(V,T) = P_{300K} + \gamma\Delta\mho_q/V \tag{23}$$

$$K_S(V,T) = K_{S\_300K} + (\gamma + 1 - q_0)\gamma\Delta\mho_q/V - \gamma^2\Delta(C_VT)/V \tag{24}$$

$$\mu(V,T) = \mu_{300K} - \eta_{S0}\Delta\mho_q/V \tag{25}$$

where P_{300K}, K_{S_300K}, and μ_{300K} are pressure, adiabatic bulk moduli, and shear moduli at 300 K, respectively, that can be calculated using Birch-Murnaghan EoS and finite-strain equations (Birch 1952), q_0 is a volume-independent constant, γ is the Grüneisen parameter, η_{S0} is the shear strain derivative of γ, and $\Delta\mho_q$ and $\Delta(C_VT)$ are internal energy and heat differences between 300 K and high temperature, respectively. γ and α can be calculated using equations of $\gamma = \gamma_0(V/V_0)^{q0}$ and $\alpha = 1/V(\partial V/\partial T)_P$. High P-T $\mho_q$ and isochoric heat capacity (C_V) can be modeled with Debye approximations:

$$\mho_q(V,T) = 9nRT\left(\frac{\theta_D}{T}\right)^{-3}\int_0^{\theta_D/T}\frac{x^3}{e^x-1}dx \tag{26}$$

$$C_V(V,T) = 9nRT\left(\frac{\theta_D}{T}\right)^{-3}\int_0^{\theta_D/T}\frac{x^4e^x}{\left(e^x-1\right)^2}dx \tag{27}$$

where R is the gas constant, n is the number of atoms in the mineral formula, and θ_D is Debye temperature, expressed as:

$$\theta_D = \theta_0 e^{\left(-\frac{\gamma-\gamma_0}{q_0}\right)} \tag{28}$$

TABLE 3. Comparisons of bulk and shear moduli of bridgmanite and their pressure derivatives at room temperature

Brillouin light scattering	Composition	K_{S0} (GPa)	μ_0 (GPa)	K'_{S0}	μ'_0
This study[a]	$Mg_{0.93}Fe^{3+}_{0.048}Fe^{2+}_{0.032}Al_{0.10}Si_{0.90}O_3$	326(4)	211(2)	3.32(4)	1.66(2)
Fu et al. (2018)	$Mg_{0.96(1)}Fe^{2+}_{0.036(5)}Fe^{3+}_{0.014(5)}Si_{0.99(1)}O_3$ (<42.6 GPa)	254(8)	166.2(5)	3.3(3)	1.91(2)
Fu et al. (2018)	$Mg_{0.96(1)}Fe^{2+}_{0.036(5)}Fe^{3+}_{0.014(5)}Si_{0.99(1)}O_3$ (>58 GPa)	234(11)	190.0(7)	3.5(4)	1.54(11)
Jackson et al. (2005)	Al-Bgm (5.1 wt% Al_2O_3)	252(5)	165(2)	3.7(3)	1.7(2)
Murakami et al. (2007)	$MgSiO_3$		172.9(2)		1.56(4)
Murakami et al. (2012)	Al-Bgm (4 wt% Al_2O_3)		166(1)		1.57(5)
Kurnosov et al. (2017)	$(Mg_{0.9}Fe_{0.1} Al_{0.1}Si_{0.9})O_3$	250.8(4)	159.7(2)	3.44(3)	2.05(2)
Criniti et al. (2021)	$MgSiO_3$	257.1(6)	175.6(2)	3.71(4)	1.86(1)

Ultrasonic interferometry	Composition	K_{S0} (GPa)	μ_0 (GPa)	K'_{S0}	μ'_0
Li and Zhang (2005)	$MgSiO_3$	253(2)	173(1)	4.4(1)	2.0(1)
Chantel et al. (2012)	$MgSiO_3$	247(4)	176(2)	4.5(2)	1.6(1)
Chantel et al. (2012)	$(Mg_{0.95}Fe_{0.05})SiO_3$	236(2)	174(1)	4.7(1)	1.56(5)

| X-ray diffraction	Composition	K_{T0} (GPa)		K'_{T0}	
This study	$Mg_{0.93}Fe^{3+}_{0.048}Fe^{2+}_{0.032}Al_{0.10}Si_{0.90}O_3$	256(2)		4 (fixed)	
Fu et al. (2018)	$Mg_{0.96(1)}Fe^{2+}_{0.036(5)}Fe^{3+}_{0.014(5)}Si_{0.99(1)}O_3$ (<40 GPa)	258(1)		4 (fixed)	
Fu et al. (2018)	$Mg_{0.96(1)}Fe^{2+}_{0.036(5)}Fe^{3+}_{0.014(5)}Si_{0.99(1)}O_3$ (>60 GPa)	252(2)		4 (fixed)	
Chantel et al. (2012)	$MgSiO_3$	257(2)		4 (fixed)	
Chantel et al. (2012)	$(Mg_{0.95}Fe_{0.05})SiO_3$	246(2)		4 (fixed)	
Boffa Ballaran et al. (2012)	$MgSiO_3$	251(2)		4.11(7)	
Boffa Ballaran et al. (2012)	$(Mg_{0.95}Fe_{0.05})SiO_3$	253(3)		3.99(7)	
Boffa Ballaran et al. (2012)	$(Mg_{0.6}Fe_{0.4})(Al_{0.36}Si_{0.62})O_3$	240(2)		4.12(8)	
Mao et al. (2017)	$(Mg_{0.94}Fe_{0.06}) (Al_{0.01}Si_{0.99})O_3$	255(2)		4 (fixed)	
Mao et al. (2017)	$(Mg_{0.89}Fe_{0.11}) (Al_{0.11}Si_{0.89})O_3$	264(2)		4 (fixed)	

[a] The reference pressure is 25 GPa.

where θ_0 is the ambient Debye temperature. Four parameters, θ_0, γ_0, q_0, and η_{S0} are involved in the high-temperature extrapolations of velocities. Here, we neglected chemical effects on these parameters for bridgmanite due to limited high P-T experimental data on different compositions. Values of θ_0, q_0, γ_0, and η_{S0} for (Al,Fe)-bearing bridgmanite are constrained as 900 K, 1.57, 1.1, and 2.4, respectively (Online Materials[1] Table S3), by benchmarking from previous experimental data together with ab initio calculations (Fiquet et al. 2000; Shim and Duffy 2000; Stixrude and Lithgow-Bertelloni 2005; Tange et al. 2012; Wentzcovitch et al. 2004; Wolf et al. 2015). We note that perturbations to these temperature-related parameters have weak influences on the modeled velocity profiles (Cottaar et al. 2014). For instance, if ±20%, ±30%, ±50%, and ±40% perturbations are given to θ_0, q_0, γ_0, and η_{S0} values, respectively, variations in v_P, v_S, and ρ will be <0.6%.

Taking advantage of quantitative Fe and Al effects on elastic properties of bridgmanite as discussed earlier, we modeled velocity profiles of bridgmanite with three compositions along an expected geotherm in the lower mantle (Katsura et al. 2010), including $MgSiO_3$ end-member, Fe5-Al5-Bgm with 5 mol% Fe and Al, and Fe10-Al10-Bgm with 10 mol% Fe and Al. Our modeled results show that the v_P and v_S of $MgSiO_3$ end-member are about 2.9 and 3.7% higher than those of PREM, respectively (Fig. 7). With the Fe and Al contents increasing in bridgmanite, both v_P and v_S decrease. For instance, the Fe5-Al5-Bgm has 1–2% higher v_P and v_S than PREM and the Fe10-Al10-Bgm show almost consistent velocities to PREM across the whole lower-mantle depth within uncertainties.

Lower-mantle mineralogy from velocity profiles of mineral aggregates

To the first order, the lower mantle is believed to be chemically homogenous, adiabatic, and under gravitational self-compression with Bullen's parameter close to one because of the consistency between 1D seismic profiles (Dziewonski and

Anderson 1981; Kennett et al. 1995) and the Adams-Williamson equation (Williamson and Adams 1923). With such a simplification, we made the following assumptions to quantitatively estimate the lower-mantle composition: (1) volume percentages of bridgmanite (V_{Bgm}), ferropericlase (V_{Fp}), and davemaoite (V_{CaPv}) are constant with depth, where the total is defined as 100%; (2) total Fe content (Fe) is constant with depth: Fe = $Fe_{Bgm}V_{Bgm} + Fe_{Fp}V_{FP}$, where Fe_{Bgm} and Fe_{Fp} are Fe contents in bridgmanite and ferropericlase, respectively; (3) Studies have
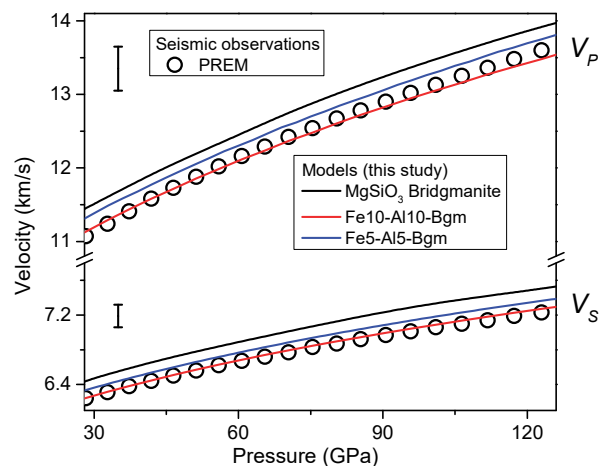

FIGURE 7. Modeled velocity profiles of bridgmanite at lower-mantle relevant pressure-temperature conditions. Using the quantitative Fe and Al effects on elastic properties of bridgmanite, we modeled v_P and v_S of three bridgmanite compositions, $MgSiO_3$ end-member (black lines), Fe5-Al5-Bgm with 5 mol% Fe and Al (blue lines), and Fe10-Al10-Bgm with 10 mol% Fe and Al (red lines) along an expected adiabatic geotherm (Katsura et al. 2010). PREM profiles (Dziewonski and Anderson 1981) are plotted as open circles for comparison. Vertical ticks show one standard deviation (±1σ) derived from standard error propagations in the modeling. (Color online.)

suggested Fe partitioning coefficient between bridgmanite and ferropericlase (K_D, given by $[Fe^{2+}+Fe^{3+}]_{Bgm}/[Mg^{2+}]_{Bgm})/(Fe^{2+}]_{Fp}/[Mg^{2+}]_{Fp})$ could vary with depth as a result of the spin crossover in ferropericlase (Irifune et al. 2010), so we used the K_D value (Fig. 8a); (4) bulk properties of mineral aggregates can be represented using Voigt-Reuss-Hill averages (Hill 1952). With all these factors considered, we have modeled v_P, v_S, and ρ profiles of bridgmanite, ferropericlase, and CaSiO₃ davemaoite aggregates along an adiabatic geotherm (Katsura et al. 2010) to best fit with seismic PREM profiles (Dziewonski and Anderson 1981) from 28 to 120 GPa. Note that we have not included the topmost and lowermost lower-mantle regions because the breakdown of majoritic garnet (Hirose et al. 2001) and large temperature gradients (Kawai and Tsuchiya 2009) can significantly affect seismic profiles in these regions, respectively. We also note that thermoelastic parameters of ferropericlase and davemaoite for high P-T modeling were constrained by refitting and benchmarking from previous experiments and theoretical calculations (see details in Online Materials[1] Figs. S2–S3 and Table S3) (Fan et al. 2019; Gréaux et al. 2019; Kawai and Tsuchiya 2015; Li et al. 2006; Sun et al. 2016; Wu et al. 2013; Yang et al. 2016)

Our best fits to PREM velocity profiles show a lower-mantle mineralogy of ~88.7(±2.0) vol% (Al,Fe)-bearing bridgmanite, ~4.3(±2.0) vol% ferropericlase, and 7 vol% (fixed) CaSiO₃ davemaoite (Fig. 8). In contrast, a pyrolitic model shows lower v_P and v_S profiles than PREM (Figs. 8e–8f). Because we varied K_D with depth in our best-fit model (Irifune et al. 2010), Fe and Al contents in bridgmanite and ferropericlase can vary accordingly (Figs. 8a–8b). For the three individual minerals, bridgmanite displays slightly higher velocities than those of PREM, while ferropericlase and CaSiO₃ davemaoite show lower velocities (Figs. 8c–8d). In comparison, velocities of bridgmanite containing fixed 10 mol% Fe and Al are barely distinguishable with PREM within uncertainties (Fig. 7). Specifically, v_S profiles of these minerals are well distinguishable from one another, which makes it the most sensitive elastic parameter to evaluate the lower-mantle mineralogy. v_P softening across the spin crossover in ferropericlase is smeared out because of the high-temperature effect in broadening the transition, but the v_P reduction within the spin crossover is still visible at mid-lower mantle P-T. Notably, the Fe content in the low-spin ferropericlase increases because of the varying K_D with depth (Fig. 8b), which in turn flattens v_S toward the deeper lower mantle (Fig. 8d). We note that in the best-fit model, we fixed the amount of davemaoite as 7 vol% because of its low abundance in both pyrolitic and chondritic models (McDonough and Sun 1995). We conducted additional fits to allow K_D and the davemaoite content to vary within 0.33–0.74 and 5–10 vol%, respectively (Online Materials[1] Fig. S4). We found that their variations have limited effects on the derived lower-mantle mineralogy (e.g., they would cause ~2 vol% variation in bridgmanite content).

The modeled high P-T v_P and v_S profiles of mineral aggregates have typical errors of ± 2–3% at ± 1σ level because of uncertainties involved in experimental data, evaluations of Fe/Al effects,
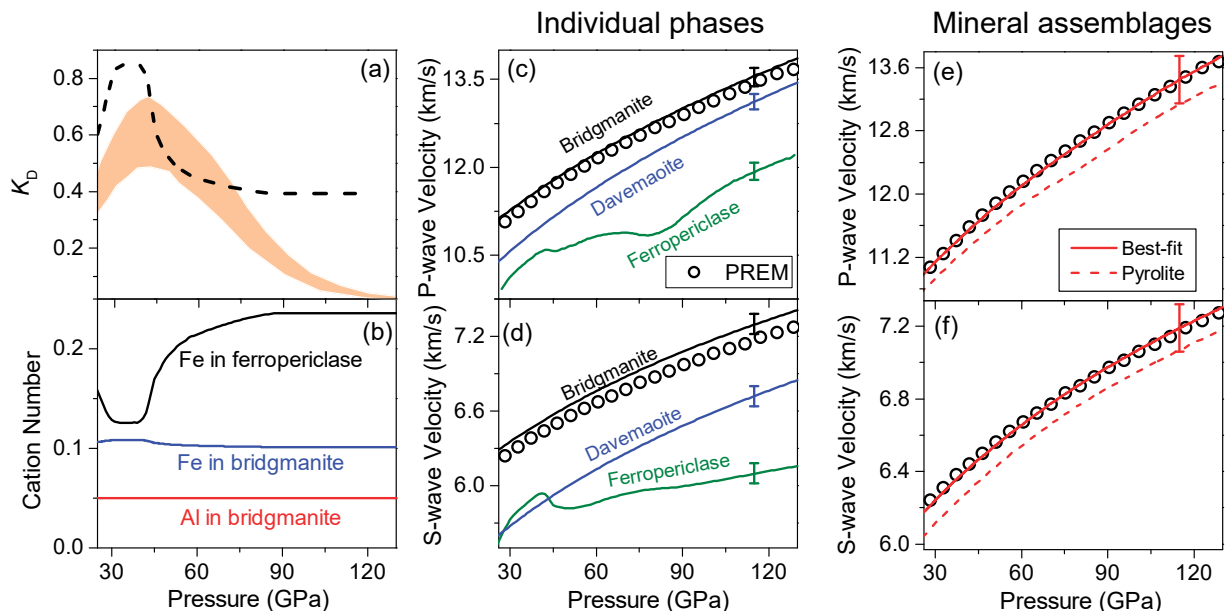
Figure 8. Lower-mantle mineralogy in the best-fit to seismic PREM profiles. (**a**) Iron partitioning between ferropericlase and bridgmanite (K_D). The dashed black line is from experiments (Irifune et al. 2010) used in this study and shaded orange area is from a theoretical report (Xu et al. 2017). (**b**) Cation numbers of Fe and Al in bridgmanite and/or ferropericlase with depth. (**c** and **d**) P-wave and S-wave velocities of individual phases, respectively, in our best-fit model. Solid black, olive and blue lines are for (Al,Fe)-bearing bridgmanite, ferropericlase, and davemaoite, respectively. The Fe/Al contents in bridgmanite/ferropericlase change with depth, shown in **b**. Velocities of individual phase were modeled along an adiabatic geotherm (Katsura et al. 2010). PREM profiles (Dziewonski and Anderson 1981) are plotted as open circles. (**e** and **f**) P-wave and S-wave velocities of mineral aggregates, respectively. Solid red lines are our best-fits to PREM (Dziewonski and Anderson 1981). Modeled results for a pyrolitic lower mantle (Irifune et al. 2010) are plotted as dashed red lines. Our best-fit model shows the lower mantle is composed of ~88.7(±2.0) vol% bridgmanite, ~4.3(±2.0) vol% ferropericlase, and 7 vol% (fixed) CaSiO₃ davemaoite. Vertical ticks show one standard deviation (±1σ) derived from standard error propagations in the modeling. (Color online.)

and high *P-T* extrapolations. Our modeling shows that a pyrolitic model with +1σ upper bounds would marginally overlap with PREM profiles (Figs. 8e–8f). In addition, although we took the adiabatic mantle geotherm from the literature (Katsura et al. 2010) in our model, thermoelastic properties of constituent materials would, in turn, affect the lower-mantle thermal status. If we assume the lower mantle is superadiabatic with the Bullen's parameter less than 1 (Bunge et al. 2001), it will consequently result in 1–2% decrease in velocities and cause additional mismatches with PREM. Overall, taking all these factors into consideration, even with the most comprehensive study on the single-crystal elasticity of (Al,Fe)-bearing bridgmanite thus far, the uncertainties (±1σ) in velocity profiles of the lower-mantle bridgmanite are in the order of a few percent. This magnitude would translate into a significant uncertainty of approximately 15 vol% in evaluating the lower-mantle compositions such as pyrolite and chondritic models (McDonough and Sun 1995; Murakami et al. 2012; Ringwood 1975). Future high *P-T* elasticity studies using combined high-quality mineral physics results with ~0.1% uncertainties and high-resolution seismic data are needed to better elucidate spatial and temporal signatures of the mantle geophysics, geodynamics, and geochemistry.

REFERENCES CITED

Allègre, C.J., Poirier, J.-P., Humler, E., and Hofmann, A.W. (1995) The chemical composition of the Earth. Earth and Planetary Science Letters, 134, 515–526, https://doi.org/10.1016/0012-821X(95)00123-T.

Birch, F. (1952) Elasticity and constitution of the Earth interior. Journal of Geophysical Research, 57, 227–286, https://doi.org/10.1029/JZ057i002p00227.

——— (1978) Finite strain isotherm and velocities for single-crystal and polycrystalline NaCl at high-pressures and 300°K. Journal of Geophysical Research: Solid Earth, 83, 1257–1268.

Boffa Ballaran, T., Kurnosov, A., Glazyrin, K., Frost, D.J., Merlini, M., Hanfland, M., and Caracas, R. (2012) Effect of chemistry on the compressibility of silicate perovskite in the lower mantle. Earth and Planetary Science Letters, 333-334, 181–190, https://doi.org/10.1016/j.epsl.2012.03.029.

Bunge, H.P., Ricard, Y., and Matas, J. (2001) Non-adiabaticity in mantle convection. Geophysical Research Letters, 28, 879–882, https://doi.org/10.1029/2000GL011864.

Chantel, J., Frost, D.J., McCammon, C.A., Jing, Z.C., and Wang, Y.B. (2012) Acoustic velocities of pure and iron-bearing magnesium silicate perovskite measured to 25 GPa and 1200 K. Geophysical Research Letters, 39(19), https://doi.org/10.1029/2012GL053075.

Cottaar, S., Heister, T., Rose, I., and Unterborn, C. (2014) BurnMan: A lower mantle mineral physics toolkit. Geochemistry, Geophysics, Geosystems, 15, 1164–1179, https://doi.org/10.1002/2013GC005122.

Criniti, G., Kurnosov, A., Boffa Ballaran, T., and Frost, D.J. (2021) Single-crystal elasticity of MgSiO₃ bridgmanite to mid-lower mantle pressure. Journal of Geophysical Research: Solid Earth, 126, e2020JB020967.

Dewaele, A., Loubeyre, P., and Mezouar, M. (2004) Equations of state of six metals above 94 GPa. Physical Review B: Condensed Matter and Materials Physics, 70, 094112, https://doi.org/10.1103/PhysRevB.70.094112.

Dziewonski, A.M. and Anderson, D.L. (1981) Preliminary reference Earth model. Physics of the Earth and Planetary Interiors, 25, 297–356, https://doi.org/10.1016/0031-9201(81)90046-7.

Every, A. (1980) General closed-form expressions for acoustic waves in elastically anisotropic solids. Physical Review B: Condensed Matter, 22, 1746–1760, https://doi.org/10.1103/PhysRevB.22.1746.

Fan, D., Fu, S., Yang, J., Tkachev, S.N., Prakapenka, V.B., and Lin, J.F. (2019) Elasticity of single-crystal periclase at high pressure and temperature: The effect of iron on the elasticity and seismic parameters of ferropericlase in the lower mantle. American Mineralogist, 104, 262–275, https://doi.org/10.2138/am-2019-6656.

Fei, Y.W., Zhang, L., Corgne, A., Watson, H., Ricolleau, A., Meng, Y., Prakapenka, V. (2007) Spin transition and equations of state of (Mg,Fe)O solid solutions. Geophysical Research Letters, 34. https://doi.org/10.1029/2007GL030712

Fiquet, G., Dewaele, A., Andrault, D., Kunz, M., and Le Bihan, T. (2000) Thermoelastic properties and crystal structure of MgSiO₃ perovskite at lower mantle pressure and temperature conditions. Geophysical Research Letters, 27, 21–24, https://doi.org/10.1029/1999GL008397.

Frost, D.J., Liebske, C., Langenhorst, F., McCammon, C.A., Trønnes, R.G., and Rubie, D.C. (2004) Experimental evidence for the existence of iron-rich metal in the Earth's lower mantle. Nature, 428, 409–412, https://doi.org/10.1038/nature02413.

Fu, S., Yang, J., Zhang, Y., Okuchi, T., McCammon, C., Kim, H.I., Lee, S.K., and Lin, J.F. (2018) Abnormal elasticity of Fe-bearing bridgmanite in the Earth's lower mantle. Geophysical Research Letters, 45, 4725–4732, https://doi.org/10.1029/2018GL077764.

Fu, S., Yang, J., Karato, S.i., Vasiliev, A., Presniakov, M.Y., Gavriliuk, A.G., Ivanova, A.G., Hauri, E.H., Okuchi, T., Purevjav, N., and others. (2019a) Water concentration in single-crystal (Al,Fe)-bearing bridgmanite grown from the hydrous melt: Implications for dehydration melting at the topmost lower mantle. Geophysical Research Letters, 46, 10346–10357, https://doi.org/10.1029/2019GL084630.

Fu, S., Yang, J., Tsujino, N., Okuchi, T., Purevjav, N., and Lin, J.F. (2019b) Single-crystal elasticity of (Al,Fe)-bearing bridgmanite and seismic shear wave radial anisotropy at the topmost lower mantle. Earth and Planetary Science Letters, 518, 116–126, https://doi.org/10.1016/j.epsl.2019.04.023.

Fukui, H., Yoneda, A., Nakatsuka, A., Tsujino, N., Kamada, S., Ohtani, E., Shatskiy, A., Hirao, N., Tsutsui, S., Uchiyama, H., and others. (2016) Effect of cation substitution on bridgmanite elasticity: A key to interpret seismic anomalies in the lower mantle. Scientific Reports, 6, 33337, https://doi.org/10.1038/srep33337.

Gréaux, S., Irifune, T., Higo, Y., Tange, Y., Arimoto, T., Liu, Z., and Yamada, A. (2019) Sound velocity of CaSiO₃ perovskite suggests the presence of basaltic crust in the Earth's lower mantle. Nature, 565, 218–221, https://doi.org/10.1038/s41586-018-0816-5.

Hill, R. (1952) The elastic behaviour of a crystalline aggregate. Proceedings of the Physical Society. Section A, 65, 349–354, https://doi.org/10.1088/0370-1298/65/5/307.

Hirose, K., Fei, Y., Ono, S., Yagi, T., and Funakoshi, K.-i. (2001) In situ measurements of the phase transition boundary in Mg₃Al₂Si₃O₁₂: Implications for the nature of the seismic discontinuities in the Earth's mantle. Earth and Planetary Science Letters, 184, 567–573, https://doi.org/10.1016/S0012-821X(00)00354-X.

Hofmann, A.W. (1997) Mantle geochemistry: The message from oceanic volcanism. Nature, 385, 219–229, https://doi.org/10.1038/385219a0.

Irifune, T., Shinmei, T., McCammon, C.A., Miyajima, N., Rubie, D.C., and Frost, D.J. (2010) Iron partitioning and density changes of pyrolite in Earth's lower mantle. Science, 327, 193–195, https://doi.org/10.1126/science.1181443.

Jackson, I. and Rigden, S.M. (1996) Analysis of PVT data: Constraints on the thermoelastic properties of high-pressure minerals. Physics of the Earth and Planetary Interiors, 96, 85–112, https://doi.org/10.1016/0031-9201(96)03143-3.

Jackson, J.M., Zhang, J., Shu, J., Sinogeikin, S.V., and Bass, J.D. (2005) High-pressure sound velocities and elasticity of aluminous MgSiO₃ perovskite to 45 GPa: Implications for lateral heterogeneity in Earth's lower mantle. Geophysical Research Letters, 32, L21305, https://doi.org/10.1029/2005GL023522.

Karki, B., Stixrude, L., Clark, S., Warren, M., Ackland, G., and Crain, J. (1997) Elastic properties of orthorhombic MgSiO₃ perovskite at lower mantle pressures. American Mineralogist, 82, 635–638, https://doi.org/10.2138/am-1997-5-623.

Katsura, T., Yoneda, A., Yamazaki, D., Yoshino, T., and Ito, E. (2010) Adiabatic temperature profile in the mantle. Physics of the Earth and Planetary Interiors, 183, 212–218, https://doi.org/10.1016/j.pepi.2010.07.001.

Kawai, K. and Tsuchiya, T. (2009) Temperature profile in the lowermost mantle from seismological and mineral physics joint modeling. Proceedings of the National Academy of Sciences, 106, 22119–22123, https://doi.org/10.1073/pnas.0905920106.

——— (2015) Small shear modulus of cubic CaSiO₃ perovskite. Geophysical Research Letters, 42, 2718–2726, https://doi.org/10.1002/2015GL063446.

Kennett, B.L.N., Engdahl, E.R., and Buland, R. (1995) Constraints on seismic velocities in the Earth from travel-times. Geophysical Journal International, 122, 108–124, https://doi.org/10.1111/j.1365-246X.1995.tb03540.x.

Kurnosov, A., Marquardt, H., Frost, D.J., Ballaran, T.B., and Ziberna, L. (2017) Evidence for a Fe³⁺-rich pyrolitic lower mantle from (Al,Fe)-bearing bridgmanite elasticity data. Nature, 543, 543–546, https://doi.org/10.1038/nature21390.

——— (2018) Kurnosov et al. reply. Nature, 564, E27–E31, https://doi.org/10.1038/s41586-018-0742-6.

Li, B.S. and Zhang, J.Z. (2005) Pressure and temperature dependence of elastic

wave velocity of MgSiO$_3$ perovskite and the composition of the lower. Physics of the Earth and Planetary Interiors, 151, 143–154, https://doi.org/10.1016/j.pepi.2005.02.004.

Li, L., Brodholt, J.P., Stackhouse, S., Weidner, D.J., Alfredsson, M., and Price, G.D. (2005) Elasticity of (Mg,Fe)(Si,Al)O$_3$-perovskite at high pressure. Earth and Planetary Science Letters, 240, 529–536, https://doi.org/10.1016/j.epsl.2005.09.030.

Li, L., Weidner, D.J., Brodholt, J., Alfè, D., Price, G.D., Caracas, R., and Wentzcovitch, R. (2006) Elasticity of CaSiO$_3$ perovskite at high pressure and high temperature. Physics of the Earth and Planetary Interiors, 155, 249–259, https://doi.org/10.1016/j.pepi.2005.12.006.

Lin, J.F., Speziale, S., Mao, Z., and Marquardt, H. (2013) Effects of the electronic spin transitions of iron in lower mantle minerals: Implications for deep mantle geophysics and geochemistry. Reviews of Geophysics, 51, 244–275, https://doi.org/10.1002/rog.20010.

Lin, J.F., Mao, Z., Yang, J., and Fu, S. (2018) Elasticity of lower-mantle bridgmanite. Nature, 564, E18–E26, https://doi.org/10.1038/s41586-018-0741-7.

Lundin, S., Catalli, K., Santillan, J., Shim, S.H., Prakapenka, V.B., Kunz, M., and Meng, Y. (2008) Effect of Fe on the equation of state of mantle silicate perovskite over 1 Mbar. Physics of the Earth and Planetary Interiors, 168, 97–102, https://doi.org/10.1016/j.pepi.2008.05.002.

Mao, Z., Lin, J.F., Liu, J., and Prakapenka, V.B. (2011) Thermal equation of state of lower-mantle ferropericlase across the spin crossover. Geophysical Research Letters, 38(23), https://doi.org/10.1029/2011GL049915.

Mao, Z., Wang, F., Lin, J.F., Fu, S., Yang, J., Wu, X., Okuchi, T., Tomioka, N., Prakapenka, V.B., Xiao, Y., and others. (2017) Equation of state and hyperfine parameters of high-spin bridgmanite in the Earth's lower mantle by synchrotron X-ray diffraction and Mössbauer spectroscopy. American Mineralogist, 102, 357–368, https://doi.org/10.2138/am-2017-5770.

Marquardt, H. and Marquardt, K. (2012) Focused ion beam preparation and characterization of single-crystal samples for high-pressure experiments in the diamond-anvil cell. American Mineralogist, 97, 299–304, https://doi.org/10.2138/am.2012.3911.

Marquardt, H., Speziale, S., Reichmann, H.J., Frost, D.J., and Schilling, F.R. (2009) Single-crystal elasticity of (Mg$_{0.9}$Fe$_{0.1}$)O to 81 GPa. Earth and Planetary Science Letters, 287, 345–352, https://doi.org/10.1016/j.epsl.2009.08.017.

Mashino, I., Murakami, M., Miyajima, N., and Petitgirard, S. (2020) Experimental evidence for silica-enriched Earth's lower mantle with ferrous iron dominant bridgmanite. Proceedings of the National Academy of Sciences, 117, 27899–27905, https://doi.org/10.1073/pnas.1917096117.

McCammon, C. (1997) Perovskite as a possible sink for ferric iron in the lower mantle. Nature, 387, 694–696, https://doi.org/10.1038/42685.

McDonough, W.F. and Sun, S.-S. (1995) The composition of the Earth. Chemical Geology, 120, 223–253, https://doi.org/10.1016/0009-2541(94)00140-4.

Murakami, M., Sinogeikin, S.V., Hellwig, H., Bass, J.D., and Li, J. (2007) Sound velocity of MgSiO$_3$ perovskite to Mbar pressure. Earth and Planetary Science Letters, 256, 47–54, https://doi.org/10.1016/j.epsl.2007.01.011.

Murakami, M., Ohishi, Y., Hirao, N., and Hirose, K. (2012) A perovskitic lower mantle inferred from high-pressure, high-temperature sound velocity data. Nature, 485, 90–94, https://doi.org/10.1038/nature11004.

Ringwood, A.E. (1975) Composition and Petrology of the Earth's Mantle, 618 p. McGraw-Hill.

Shim, S.-H. and Duffy, T.S. (2000) Constraints on the *PVT* equation of state of MgSiO$_3$ perovskite. American Mineralogist, 85, 354–363, https://doi.org/10.2138/am-2000-2-314.

Shukla, G. and Wentzcovitch, R.M. (2016) Spin crossover in (Mg,Fe^{3+})(Si,Fe^{3+})O$_3$ bridgmanite: Effects of disorder, iron concentration, and temperature. Physics of the Earth and Planetary Interiors, 260, 53–61, https://doi.org/10.1016/j.pepi.2016.09.003.

Shukla, G., Cococcioni, M., and Wentzcovitch, R.M. (2016) Thermoelasticity of Fe^{3+}- and Al-bearing bridgmanite: Effects of iron spin crossover. Geophysical Research Letters, 43, 5661–5670, https://doi.org/10.1002/2016GL069332.

Speziale, S., Zha, C.S., Duffy, T.S., Hemley, R.J., and Mao, H.k. (2001) Quasi-hydrostatic compression of magnesium oxide to 52 GPa: Implications for the pressure-volume-temperature equation of state. Journal of Geophysical Research: Solid Earth, 106, 515–528.

Speziale, S., Lee, V.E., Clark, S.M., Lin, J.F., Pasternak, M.P., and Jeanloz, R. (2007) Effects of Fe spin transition on the elasticity of (Mg,Fe)O magnesio-wüstites and implications for the seismological properties of the Earth's lower mantle. Journal of Geophysical Research: Solid Earth, 112. https://doi.org/10.1029/2006JB004730

Speziale, S., Marquardt, H., and Duffy, T.S. (2014) Brillouin scattering and its application in geosciences. Reviews in Mineralogy and Geochemistry, 78, 543–603, https://doi.org/10.2138/rmg.2014.78.14.

Stixrude, L. and Lithgow-Bertelloni, C. (2005) Thermodynamics of mantle minerals—I. Physical properties. Geophysical Journal International, 162, 610–632, https://doi.org/10.1111/j.1365-246X.2005.02642.x.

Sun, N., Mao, Z., Yan, S., Wu, X., Prakapenka, V.B., and Lin, J.F. (2016) Confirming a pyrolitic lower mantle using self-consistent pressure scales and new constraints on CaSiO$_3$ perovskite. Journal of Geophysical Research: Solid Earth, 121, 4876–4894, https://doi.org/10.1002/2016JB013062.

Tange, Y., Kuwayama, Y., Irifune, T., Funakoshi, K.i., and Ohishi, Y. (2012) *P-V-T* equation of state of MgSiO$_3$ perovskite based on the MgO pressure scale: A comprehensive reference for mineralogy of the lower mantle. Journal of Geophysical Research: Solid Earth, 117 (B6), https://doi.org/10.1029/2011JB008988.

Thomson, A.R., Crichton, W.A., Brodholt, J.P., Wood, I.G., Siersch, N.C., Muir, J.M.R., Dobson, D.P., and Hunt, S.A. (2019) Seismic velocities of CaSiO$_3$ perovskite can explain LLSVPs in Earth's lower mantle. Nature, 572, 643–647, https://doi.org/10.1038/s41586-019-1483-x.

Tschauner, O., Huang, S., Yang, S., Humayun, M., Liu, W., Gilbert Corder, S.N., Bechtel, H.A., Tischler, J., and Rossman, G.R. (2021) Discovery of davemaoite, CaSiO$_3$-perovskite, as a mineral from the lower mantle. Science, 374, 891–894, https://doi.org/10.1126/science.abl8568.

Wentzcovitch, R.M., Karki, B.B., Cococcioni, M., and de Gironcoli, S. (2004) Thermoelastic properties of MgSiO$_3$-perovskite: Insights on the nature of the Earth's lower mantle. Physical Review Letters, 92, 018501, https://doi.org/10.1103/PhysRevLett.92.018501.

Williamson, E.D. and Adams, L.H. (1923) Density distribution in the Earth. Journal of the Washington Academy of Sciences, 13, 413–428.

Wolf, A.S., Jackson, J.M., Dera, P., and Prakapenka, V.B. (2015) The thermal equation of state of (Mg,Fe)SiO$_3$ bridgmanite (perovskite) and implications for lower mantle structures. Journal of Geophysical Research: Solid Earth, 120, 7460–7489, https://doi.org/10.1002/2015JB012108.

Wu, Z., Justo, J.F., and Wentzcovitch, R.M. (2013) Elastic anomalies in a spin-crossover system: Ferropericlase at lower mantle conditions. Physical Review Letters, 110, 228501, https://doi.org/10.1103/PhysRevLett.110.228501.

Xu, S., Lin, J.F., and Morgan, D. (2017) Iron partitioning between ferropericlase and bridgmanite in the Earth's lower mantle. Journal of Geophysical Research: Solid Earth, 122, 1074–1087, https://doi.org/10.1002/2016JB013543.

Yang, J., Tong, X., Lin, J.F., Okuchi, T., and Tomioka, N. (2015) Elasticity of ferropericlase across the spin crossover in the Earth's lower mantle. Scientific Reports, 5, 17188, https://doi.org/10.1038/srep17188.

Yang, J., Lin, J.F., Jacobsen, S.D., Seymour, N.M., Tkachev, S.N., and Prakapenka, V.B. (2016) Elasticity of ferropericlase and seismic heterogeneity in the Earth's lower mantle. Journal of Geophysical Research: Solid Earth, 121, 8488–8500, https://doi.org/10.1002/2016JB013552.

Yeganeh-Haeri, A. (1994) Synthesis and re-investigation of the elastic properties of single-crystal magnesium silicate perovskite. Physics of the Earth and Planetary Interiors, 87, 111–121, https://doi.org/10.1016/0031-9201(94)90025-6.

Endnote: